

# Firing pattern in a memristive Hodgkin–Huxley circuit: Numerical simulation and analog circuit validation

Quan Xu, Yiteng Wang, Bei Chen, Ze Li, Ning Wang<sup>\*</sup>

School of Microelectronics and Control Engineering, Changzhou University, Changzhou 213159, PR China

## ARTICLE INFO

### Keywords:

Hodgkin–Huxley circuit  
Ion channel  
Locally active memristor  
Firing pattern  
Analog implementation

## ABSTRACT

Spiking firing patterns and their hardware implementation can assist us in exploring spike-based applications. The classical Hodgkin–Huxley circuit can generate spiking firing patterns, but it is hard to implement on analog platform because of the involvement of complex exponential nonlinearities for characterizing the sodium and potassium ion channels. To solve this issue, this paper proposes a second-order local active memristor (LAM) and a first-order LAM to respectively characterize the sodium and potassium ion channels in the Hodgkin–Huxley circuit, thereby obtains a memristive Hodgkin–Huxley circuit. Numerical simulations demonstrate that the memristive Hodgkin–Huxley circuit can generate abundant spiking firing patterns, i.e. periodic and chaotic spiking firing patterns. These abundant firing patterns can be effectively regulated by memristor- and stimulus-related parameters. Moreover, a PCB-based analog circuit employing off-the-shelf discrete circuit components is manually constructed and hardware experiments are executed. Experimental results captured from hardware measurements satisfactorily verify the numerically simulated spiking firing patterns and effectively exhibit the availability of the memristive Hodgkin–Huxley circuit in generating spiking firing patterns.

## 1. Introduction

Since the Hodgkin–Huxley circuit was created according to the significant finding of electrophysiological ion transport mechanism, various researches in neuron models [1,2], neural networks [3,4], and coupled neural networks [5,6] have attracted wide attention, which plays significant role in promoting the development of neuron-based and neural network-based applications [7]. Biological neurons are the fundamental information handing and integrating units of a nervous system [8–10]. It has been declared that dynamical characteristics of the biological neurons play a vital role in restricting biological response and understanding cognitive behaviors of the nervous systems, but explicit relation between the dynamical characteristics and the cognitive function have not been well-established [11]. In the recent past, some researchers have focused their attention on modeling the biological neurons and disclosing their dynamical characteristics [12,13]. These can help us to well understand the dynamical effects of the electrophysiological environments and revealing their generating mechanisms [14–17]. Besides, hardware implementations and experimental measurements are available ways to further investigate and reproduce neuron firing patterns [18–21]. Three ways are frequently utilized to implement neuromorphic circuits, those are, equivalent realized neuron by discrete circuit components [21–23], silicon-based neuron by complementary metal oxide semiconductor (CMOS) and bipolar transistor [24,

25], and neuristor by physical memristor and discrete circuit components [26,27]. The neuromorphic circuits implemented by these ways can generate abundant spiking firing patterns. Especially, the spiking firing patterns and their hardware implementations can assist us in exploring spike-based applications [28,29].

Memristor is an available candidate in constructing neuromorphic circuits to reproduce biological firing patterns [30–36] since its instinct superiorities of plasticity and memorability [37,38]. In these neuromorphic circuits, memristors are employed to characterize plastic synapse [30–33], electromagnetic induction [34,35], and ion channel [36], just to name a few. In particular, the local active memristor (LAM) possesses negative differential conductance, which is regarded as the newly candidate in generating action potentials [39]. Namely, LAM is the kernel of a neuron to trigger the spiking firing patterns, since local activity is the origin of spikes [40]. Up to date, the LAMs, e.g., N-type memristor [41], S-type memristor [42], and Chua Corsage memristors [43,44], were employed to directly construct memristive neuromorphic circuits to generate spiking and bursting firing patterns [45,46]. Memristor emulators are frequently involved to implement these memristive neuromorphic circuits [41,46] since the physical memristor is commercially unavailable in the form of independent device at present. Thus, the implementation of memristor emulator-based

<sup>\*</sup> Corresponding author.

E-mail address: [cczuwangning@163.com](mailto:cczuwangning@163.com) (N. Wang).

neuromorphic circuit is still an open issue in the near future. Besides, these memristive neuromorphic circuits can also generate abundant firing patterns and have the advantages of flexibility in analog design and easy-to-adjust in hardware experiment.

Hodgkin–Huxley equation and its associated Hodgkin–Huxley circuit were firstly raised to reproduce the membrane potential of squid giant axon and they were built according to the significant finding of electrophysiological ion transport mechanism [47]. Briefly, the electrophysiological ion transport mechanism based on membrane theory declares that the action potential mainly depends on a rapid sequence of changes in the permeability to the sodium and potassium ions [48]. In the classical Hodgkin–Huxley circuit, two time-varying resistors were employed to depict the electrical relations between membrane potential and the sodium ion current and potassium ion current, respectively. Till now, many silicon-based Hodgkin–Huxley neurons employing CMOS and bipolar transistor have been implemented from the viewpoints of the Hodgkin–Huxley equation emulation [49,50] and the dynamical behavior depiction [24,25]. These silicon-based Hodgkin–Huxley neurons can effectively reproduce the firing patterns exhibited in the Hodgkin–Huxley equation and can trigger more rich firing patterns. Moreover, the memristor devices were employed to physically construct scalable simplified Hodgkin–Huxley neurons [26,27] and quasi-Hodgkin–Huxley neuron [51], which can effectively generate spiking firing patterns. Besides, FPGA-based digital implementation of the Hodgkin–Huxley neuron model has been reported by fully considering the advantages of FPGA's high speed and low digital resources [52]. The analog and digital implementations are two effective ways to reproduce the neuron firing patterns.

These Hodgkin–Huxley neurons with or without memristors play a vital role in generating neuron dynamical behaviors and spike-based applications, e.g. spiking neural network with a long short-memory for artificial intelligence applications. It is worth noting that memristor emulator-based Hodgkin–Huxley circuit has not been reported yet, which deserves the researchers' concern. The memristor emulator itself, with a continuous-time model, can avoid the emergence of the computation errors in discretization processing of a digital simulator. It is worth noting that the analog circuit experiments are one of the essentials to confirm model validity and inherently complement with the numerical simulations of physical systems [53], i.e., optical microring resonators [54].

Actually, the Hodgkin–Huxley equation and circuit were built by empirical method and they lack a sound circuit-theoretic foundation [55]. In 2012, a pioneer work declared that the intrinsic properties of the two time-varying resistors satisfy the definition of LAM from the viewpoint of circuit theory [40]. The work has demonstrated that action potential generated from the Hodgkin–Huxley circuit emerges near the edge of chaos in the theoretical and numerical surveys. The edge of chaos exists in the subsets of locally active domains of the two LAMs [56]. However, the state equations of the two LAMs are described by complex exponential functions [47], which makes difficulty in implementing the Hodgkin–Huxley circuit on analog level. Inspired by the pioneer work, we propose two LAMs with simple mathematical models and implementable analog circuit to characterize the sodium and potassium ion channels in Hodgkin–Huxley circuit. To our best knowledge, there has no such memristive Hodgkin–Huxley circuit been reported yet. Herein, we are not aiming at emulating the spiking firing patterns in the classical Hodgkin–Huxley circuit, but focus on revealing abundant firing patterns in our proposed memristive Hodgkin–Huxley circuit. In other words, the primary target of building the memristive Hodgkin–Huxley circuit is to generate spiking firing patterns from a potential application perspective. These spiking firing patterns hold the promise to provide high energy efficient implementations of spike-based neuromorphic hardware for spiking neural networks [28,57].

The reminder of this paper is arranged as follows. Section 2 proposes two LAMs to characterize ion channels and thereby builds a LAM-based

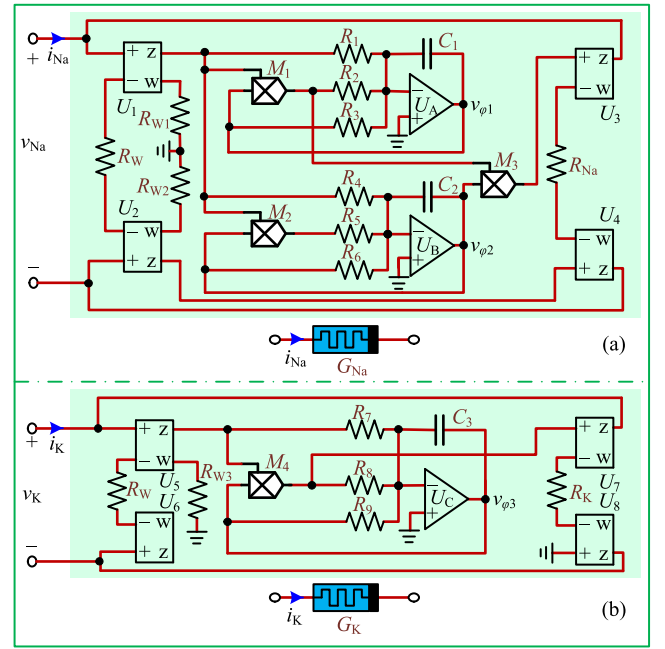


Fig. 1. Circuit schematics of the two LAMs: (a) second-order LAM to characterize sodium ion channel; (b) first-order LAM to characterize potassium ion channel.

memristive Hodgkin–Huxley circuit. Section 3 uncovers the dynamical behaviors and firing patterns related to memristor and stimulus parameters. Section 4 executes analog implementation and hardware experiments to verify the firing patterns. Finally, a brief conclusion is summarized in Section 5.

## 2. LAM-based memristive Hodgkin–Huxley circuit

To characterize the sodium and potassium ion channels in Hodgkin–Huxley circuit, a second-order LAM and a first-order LAM are proposed, thereby a memristive Hodgkin–Huxley circuit is constructed by employing the two LAMs. Firstly, equivalent circuit implemented by discrete circuit complements of the two LAMs with their frequency-dependent pinched hysteresis loops and local direct current (DC)  $V-I$  curves are demonstrated. Then, the memristive Hodgkin–Huxley circuit is constructed and its state equation is built in this section.

The equivalent circuits of the second-order LAM and first-order LAM are respectively figured out as shown in Fig. 1(a) and (b), which are implemented by off-the-shelf circuit components. It is worth stressed that the two LAMs should be no grounded limitation since the involvement of reversal potentials of sodium and potassium ion channels in classical Hodgkin–Huxley circuit. Therefore, equivalent circuits of the second-order LAM and the first-order LAM respectively contain operational amplifiers  $U_1$  to  $U_4$  and  $U_5$  to  $U_8$  to realize floating memristor and they are current feedback operational amplifier (CFOA) AD844AN [58]. The CFOA AD844AN has two input pins of inverting and noninverting input pins (marked by  $-$  and  $+$ ) and two output pins (marked by  $z$  and  $w$ ). A current applied to the inverting input pin is transferred to a complementary pair of unity-gain current mirrors that deliver the same current to an internal node (pin  $z$ ) at which the full output voltage is generated. The voltage of output pin  $w$  is equal to the one of pin  $z$ . Note that the circuit implementations for floating designs of the two LAMs are different. One is that the output pin  $z$  of  $U_2$  is connected to the noninverting input pin ( $+$ ) of  $U_4$ , while the noninverting input pin ( $+$ ) of  $U_8$  is directly grounded. The other is that the two output pins  $w$  of  $U_1$  and  $U_2$  are connected to two resistors  $R_{W1}$  and  $R_{W2}$ , which can guarantee the voltage of output pin  $z$  of  $U_2$  as  $(-R_{W2}v_{Na}/R_W)$ . However, there is no require to output the reverse voltage related to  $v_K$ . Thus,

the resistor  $R_{W3}$  is directly grounded. These designs fully employ the advantages of the CFOA AD844AN.

In detail, Fig. 1(a) demonstrates the circuit schematic for the second-order memristor, which contains two capacitors  $C_1$  and  $C_2$ , three multipliers  $M_1$ ,  $M_2$ , and  $M_3$ , two operational amplifiers  $U_A$ , and  $U_B$ , and some resistors. The circuit possess two dynamic components. Then we obtain the circuit state equations as

$$\begin{cases} i_{Na} = -\frac{g_1 g_3 v_{\varphi_1} v_{\varphi_2} R_{W1} v_{Na} + R_{W2} v_{Na}}{R_{Na} R_W}, \\ C_1 \frac{dv_{\varphi_1}}{dt} = -\frac{g_1 v_{\varphi_1} R_{W1} v_{Na}}{R_2 R_W} - \frac{v_{\varphi_1}}{R_3} - \frac{R_{W1} v_{Na}}{R_1 R_W}, \\ C_2 \frac{dv_{\varphi_2}}{dt} = -\frac{g_2 v_{\varphi_2} R_{W1} v_{Na}}{R_5 R_W} - \frac{v_{\varphi_2}}{R_6} - \frac{R_{W1} v_{Na}}{R_4 R_W}, \end{cases} \quad (1)$$

where  $v_{\varphi_1}$  and  $v_{\varphi_2}$  are the memristor inner state variables.  $v_{Na}$  and  $i_{Na}$  are the input voltage and passing current of the second-order memristor, respectively.  $g_1$ ,  $g_2$ , and  $g_3$  are gains of the three multipliers  $M_1$ ,  $M_2$ , and  $M_3$ , respectively.

In Fig. 1(b), circuit schematic for the first-order memristor is exhibited. The circuit contains a capacitor  $C_3$ , a multiplier  $M_4$ , and an operational amplifier  $U_C$ . The circuit possess two dynamic components, and then circuit state equation can be expressed as

$$\begin{cases} i_K = -\frac{g_4 v_{\varphi_3} R_{W3} v_K}{R_K R_W}, \\ C_3 \frac{dv_{\varphi_3}}{dt} = -\frac{g_4 v_{\varphi_3} R_{W3} v_K}{R_8 R_W} - \frac{v_{\varphi_3}}{R_9} - \frac{R_{W3} v_K}{R_7 R_W}, \end{cases} \quad (2)$$

where  $v_{\varphi_3}$  is memristor inner state variable.  $v_K$  and  $i_K$  are the input voltage and pass current of the first-order memristor, respectively.  $g_4$  is the gain of multiplier  $M_4$ .

The typical circuit parameters of the two LAMs are determined as  $R_W = R_5 = R_8 = R_9 = 10 \text{ k}\Omega$ ,  $R_{W1} = R_{W2} = R_{W3} = R_2 = R_4 = R_7 = 1 \text{ k}\Omega$ ,  $R_1 = 20 \text{ k}\Omega$ ,  $R_3 = R_6 = 2 \text{ k}\Omega$ ,  $g_1 = g_2 = g_4 = -1$ ,  $g_3 = 1$ ,  $C_1 = C_2 = C_3 = 10 \text{ nF}$ ,  $R_{Na} = 0.95 \text{ k}\Omega$ , and  $R_K = 1 \text{ k}\Omega$ . To disclose the frequency-dependent pinched hysteresis loops of the two memristors, a sinusoidal voltage  $v_{Na} = v_K = 5 \sin(2\pi f t) \text{ V}$  is applied to their input terminals, respectively. When  $f$  is set to 2 kHz, to 5 kHz, and to 10 kHz, the voltage-current relations of the two memristors are demonstrated in Fig. 2(a1) and (a2). The numerical results exhibit that the hysteresis loops are pinched at the origin and asymmetric, and the lobe areas decrease with the increase of the frequency. Thus, the terminal characteristics satisfy the features of memristor and they are generic memristor actually.

The DC  $V-I$  curve can intuitively exhibit local active domains of a LAM [39]. By setting  $dv_{\varphi_1}/dt = dv_{\varphi_2}/dt = 0$  and denoting  $i_{Na}$  to  $I_{Na}$  and  $v_{Na}$  to  $V_{Na}$  in (1), one can get

$$\begin{cases} I_{Na} = -\frac{g_1 g_3 v_{\varphi_1} v_{\varphi_2} R_{W1} V_{Na} + R_{W2} V_{Na}}{R_{Na} R_W}, \\ 0 = -\frac{g_1 v_{\varphi_1} R_{W1} V_{Na}}{R_2 R_W} - \frac{v_{\varphi_1}}{R_3} - \frac{R_{W1} V_{Na}}{R_1 R_W}, \\ 0 = -\frac{g_2 v_{\varphi_2} R_{W1} V_{Na}}{R_5 R_W} - \frac{v_{\varphi_2}}{R_6} - \frac{R_{W1} V_{Na}}{R_4 R_W}, \end{cases} \quad (3)$$

Similarly, by setting  $dv_{\varphi_3}/dt = 0$  and denoting  $i_K$  to  $I_K$  and  $v_K$  to  $V_K$  in (2), one can get

$$\begin{cases} I_K = -\frac{g_4 v_{\varphi_3} R_{W3} V_K}{R_K R_W}, \\ 0 = -\frac{g_4 v_{\varphi_3} R_{W3} V_K}{R_8 R_W} - \frac{v_{\varphi_3}}{R_9} - \frac{R_{W3} V_K}{R_7 R_W}, \end{cases} \quad (4)$$

Considering  $V_{Na}$  and  $V_K$  adjusted in the region  $[-5, 3]$ , the local DC  $V-I$  curves of the second-order and the first-order memristors are figured out by numerical method as demonstrated in Fig. 2(b1) and (b2), respectively. The DC  $V_{Na} - I_{Na}$  curve is single-valued and

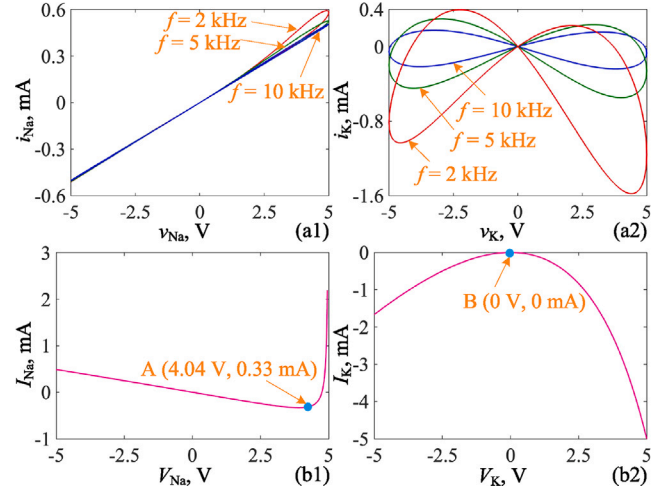


Fig. 2. Frequency-dependent pinched hysteresis loops and local DC  $V-I$  curves of the two LAMs: (a1) and (a2) frequency-dependent pinched hysteresis loops for  $f = 2 \text{ kHz}$ ,  $5 \text{ kHz}$ , and  $10 \text{ kHz}$ ; (b1) and (b2) local DC  $V-I$  curve.

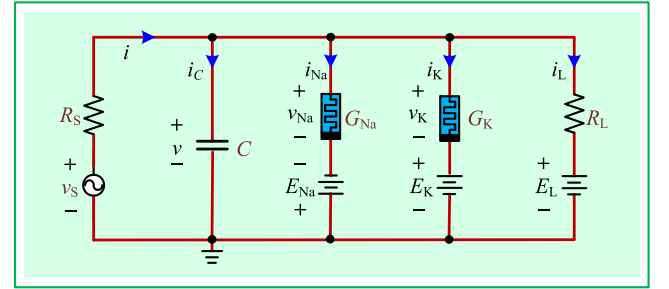


Fig. 3. Circuit schematic of the proposed memristive Hodgkin-Huxley circuit.

demonstrates negative slope when  $V_K < 4.04 \text{ V}$  (curve located at the left of point A). Thus, the proposed second-order memristor is locally active. For the first-order memristor, the DC  $V_K - I_K$  curve is also single-valued and displays negative slope when  $V_K > 0$  (curve located at the right of point B). Thus, the proposed first-order memristor is also locally active. Summarily, the second-order LAM can run in locally active domain when applying a DC bias under  $4.04 \text{ V}$  and the first-order LAM can run in locally active domain when applying a positive DC bias. Aka, the two memristors are local active with negative differential conductance. Thus, the two LAMs are dubbed “edge of chaos kernel” as the newly candidate in generating firing patterns [55].

Afterwards, a memristive Hodgkin-Huxley circuit is newly built by employing the second-order LAM and first-order LAM to characterize the sodium and potassium ion channels, respectively. The memristive Hodgkin-Huxley circuit shown in Fig. 3 contains a membrane capacitor  $C$ , the two LAMs  $G_{Na}$  and  $G_K$ , three reversal potentials  $E_{Na}$ ,  $E_K$ , and  $E_L$  of sodium, potassium, and leakage ion channels, a leakage resistor  $R_L$ , and an externally applied stimulus  $v_s$  with its series connecting resistor  $R_s$ , respectively. Herein, taking the consideration of feasibility in hardware implementation, we employ voltage source to replace the current stimulus in classical Hodgkin-Huxley circuit [47]. The memristive Hodgkin-Huxley circuit with the two LAMs contains four capacitors possessing four state variables. Employ the Kirchhoff's Laws and constitutive relation of circuit elements, we can obtain circuit state

equation of the memristive Hodgkin–Huxley circuit as

$$\begin{cases} C \frac{dv}{dt} = \frac{v_S - v}{R_S} + \frac{g_1 g_3 v_{\phi_1} v_{\phi_2} R_{W1}(v + E_{Na}) + R_{W2}(v + E_{Na})}{R_{Na} R_W} \\ \quad + \frac{g_4 v_{\phi_3} R_{W3}(v - E_K)}{R_K R_W} - \frac{v - E_L}{R_L}, \\ C_1 \frac{dv_{\phi_1}}{dt} = -\frac{g_1 v_{\phi_1} R_{W1}(v + E_{Na})}{R_2 R_W} - \frac{v_{\phi_1}}{R_3} - \frac{R_{W1}(v + E_{Na})}{R_1 R_W}, \\ C_2 \frac{dv_{\phi_2}}{dt} = -\frac{g_2 v_{\phi_2} R_{W1}(v + E_{Na})}{R_5 R_W} - \frac{v_{\phi_2}}{R_6} - \frac{R_{W1}(v + E_{Na})}{R_4 R_W}, \\ C_3 \frac{dv_{\phi_3}}{dt} = -\frac{g_4 v_{\phi_3} R_{W3}(v - E_K)}{R_8 R_W} - \frac{v_{\phi_3}}{R_9} - \frac{R_{W3}(v - E_K)}{R_7 R_W}, \end{cases} \quad (5)$$

where  $v$  is the membrane potential. The externally applied stimulus has the form of  $v_S = V_m \sin(2\pi f t)$ . The other typical circuit parameters of the memristive Hodgkin–Huxley circuit are determined as  $R_S = 10 \text{ k}\Omega$ ,  $R_L = 100 \text{ k}\Omega$ ,  $C = 10 \text{ nF}$ ,  $E_{Na} = 1 \text{ V}$ ,  $E_K = 0.8 \text{ V}$ ,  $E_L = 2 \text{ V}$ ,  $V_m = 2 \text{ V}$ , and  $f = 1 \text{ kHz}$ . Note that the reversal potentials  $E_{Na}$  and  $E_K$  can push the two LAMs into their local active domains, respectively.

### 3. Parameter-dependent dynamical behaviors

The electrophysiological properties of sodium and potassium ion channels effectively determine the firing pattern of biological neuron [48,59]. What is more, the externally applied electrical stimulus can intensively affect the electrophysiological response of biological neurons [60–63]. In this section, we mainly explore the dynamics of the memristive Hodgkin–Huxley circuit related to memristor parameters  $R_{Na}$  and  $R_K$ , as well as the stimulus parameters  $A$  and  $f$ . In numerical simulations, MATLAB-based ODE45 algorithm with time-step  $10^{-6} \text{ s}$  and time-end  $0.1 \text{ s}$  is employed to calculate bifurcation diagram, as well as the Jacobi matrix-based Wolf's method with time-step  $10^{-4} \text{ s}$  and time-end  $2 \text{ s}$  is utilized to calculate Lyapunov exponent. Besides, the initial conditions  $[v(0), v_{\phi_1}(0), v_{\phi_2}(0), v_{\phi_3}(0)] = [0 \text{ V}, 0 \text{ V}, 0 \text{ V}, 0 \text{ V}]$  are assigned.

#### 3.1. Memristor parameter-dependent dynamical behaviors

The 2D bifurcation diagram can focus on the dynamical distribution of firing patterns in two parameters plane. To simultaneously explore the dynamical effects of sodium and potassium ion channels, we investigate the dynamical distribution in the  $R_{Na} - R_K$  parameter plane. Herein, the memristor parameters  $R_{Na}$  and  $R_K$  are scanned in  $0.8 \text{ k}\Omega \leq R_{Na} \leq 1.6 \text{ k}\Omega$  with step  $1.6 \text{ }\Omega$  and  $0.8 \text{ k}\Omega \leq R_K \leq 1.1 \text{ k}\Omega$  with step  $0.6 \text{ }\Omega$ , respectively. The 2D bifurcation diagram is depicted by checking the periodicities of the membrane potential  $v$  as shown in Fig. 4(a). Different parameter regions are painted by different colors to distinguish firing patterns, those are, the yellow regions marked by CH represents chaos, the purple regions marked by MP stands for periodic state with periodicities more than 8, and the other colorful regions marked by P1 to P8 represent period-1 to period-8, respectively. Some regions are very narrow, but we confirm the existence of these firing patterns by numerical simulations. One can see that numerous ribbons marked by P3, P5, and P7 are embed in CH (yellow) regions. This declares that numerous periodic windows are triggered by varying the two LAM-related parameters. These periodic windows are generated via tangent bifurcations and disappeared via chaos crisis [29].

Besides, 2D dynamical map described by the largest Lyapunov exponent (LLE) is an available method to confirm the dynamical distribution in 2D parameter plane for a dynamical system. 2D dynamical map in the  $R_{Na} - R_K$  parameter plane are figured out in Fig. 4(b). They are painted by different colors according to the values of LLE, those are red for chaos with positive LLE and other colors for period with negative LLE [22]. Compare Fig. 4(a) with (b), one can see that the dynamical behaviors depicted by 2D bifurcation diagrams are the same as those revealed by the 2D dynamical map.

To clearly demonstrate the transition process of firing patterns, 1D bifurcation diagram and LLE spectrum are simulated with respect to memristor parameters  $R_{Na}$  and  $R_K$  as shown in Fig. 5(a) and (b), respectively. Herein,  $R_{Na}$  is adjusted in the region  $[0.8 \text{ k}\Omega, 1.6 \text{ k}\Omega]$  with  $R_{Na} = 1 \text{ k}\Omega$ ,  $A = 2 \text{ V}$ , and  $f = 1 \text{ kHz}$  and  $R_K$  is adjusted in the region  $[0.8 \text{ k}\Omega, 1.1 \text{ k}\Omega]$  with  $R_{Na} = 0.95 \text{ k}\Omega$ ,  $A = 2 \text{ V}$ , and  $f = 1 \text{ kHz}$ , respectively. The tops of Fig. 5(a) and (b) display the 1D bifurcation diagrams of membrane potential  $v$  while the bottoms exhibit LLE spectra. Note that the LLE spectra in some parameter regions are omitted since the values of LLEs in these parameter regions are very small. One can see that the transitions of firing patterns are rather complex, which trigger the generation of rich firing patterns, i.e. periodic firing patterns with different periodicities and chaotic firing pattern. The bifurcation diagrams can more clearly demonstrate the existence of tangent bifurcation and chaos crisis.

These numerical simulations demonstrate that the LAM-related parameters can effectively affect the firing pattern of the memristive Hodgkin–Huxley circuit. This reflects that the electrical characteristics of sodium and potassium ion channels can influence firing activities of the biological neurons from an electrophysiological perspective. Besides, the abundant firing patterns generated in the memristive Hodgkin–Huxley circuit can be effectively regulated by the LAM-related parameters, which can provide potential application in spiking neuronal network.

#### 3.2. Stimulus parameter-dependent dynamical behaviors

Biological experiments have manifested that externally applied stimulus can intensively affect the electrophysiological response of biological neurons in human brain [60,61]. In modeling these electrophysiological processes, DC current and pulse current stimuli, Wiener-noise, and White-noise are frequently employed [62–66]. Actually, the electromagnetic radiation can also influence the electrical activity of a biological neuron, and then alter the behavior of the nervous system [67,68]. Thus, the externally applied stimulus induced dynamical behaviors, i.e. stimulus amplitude- and frequency-related dynamics, are numerically explored.

When amplitude and frequency of the externally applied stimulus are adjusted in  $0 \text{ V} \leq A \leq 5 \text{ V}$  and  $0.5 \text{ kHz} \leq f \leq 2 \text{ kHz}$ , dynamical distributions in the  $A - f$  parameter plane are demonstrated in Fig. 6. The color settings of the 2D bifurcation diagram in Fig. 6(a) are identical as those utilized in Fig. 4(a). The 2D bifurcation diagram demonstrates more complex ribbon structure, which manifests the generations of periodic window via tangent bifurcation and chaos crisis with variations of the two stimulus-related parameters  $A$  and  $f$ . In Fig. 6(b), the 2D dynamical map further confirms the dynamical distribution disclosed by the 2D bifurcation diagram. These dynamical distributions indicate the generation of rich stimulus-related dynamical behaviors in the memristive Hodgkin–Huxley circuit.

Furthermore, bifurcation behaviors with respect to amplitude  $A$  and frequency  $f$  are respectively demonstrated by 1D bifurcation diagram and LLE spectrum. The 1D bifurcation diagrams and LLE spectra are depicted for  $0 \text{ V} \leq A \leq 5 \text{ V}$  with  $f = 1 \text{ kHz}$  and for  $0.5 \text{ kHz} \leq f \leq 2 \text{ kHz}$  with  $A = 2 \text{ V}$  as shown in Fig. 7(a) and (b) respectively. One can see that abundant periodic behaviors having different periodicities and chaos are also emerged with the adjustments of amplitude  $A$  and frequency  $f$ . These numerical results exhibit that the external stimulus can intensively influence the bifurcation behaviors of the memristive Hodgkin–Huxley circuit, leading to the generation of periodic and chaotic firing patterns. This reflects that firing patterns of a biological neuron can be triggered and regulated by externally applied stimulus.



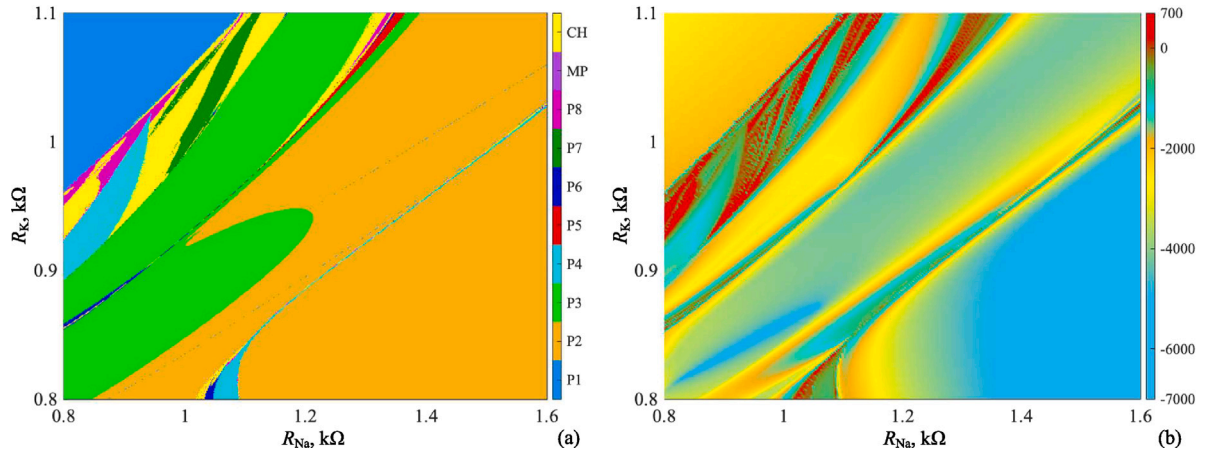


Fig. 4. Memristor parameter-related dynamical distributions in the  $R_{Na}$ - $R_K$  parameter plane: (a) 2D bifurcation diagram depicted by checking periodicities of the membrane potential  $v_i$ ; (b) 2D dynamical map described by LLE. (For interpretation of the references to color in this figure legend, the reader is referred to the web version of this article.)

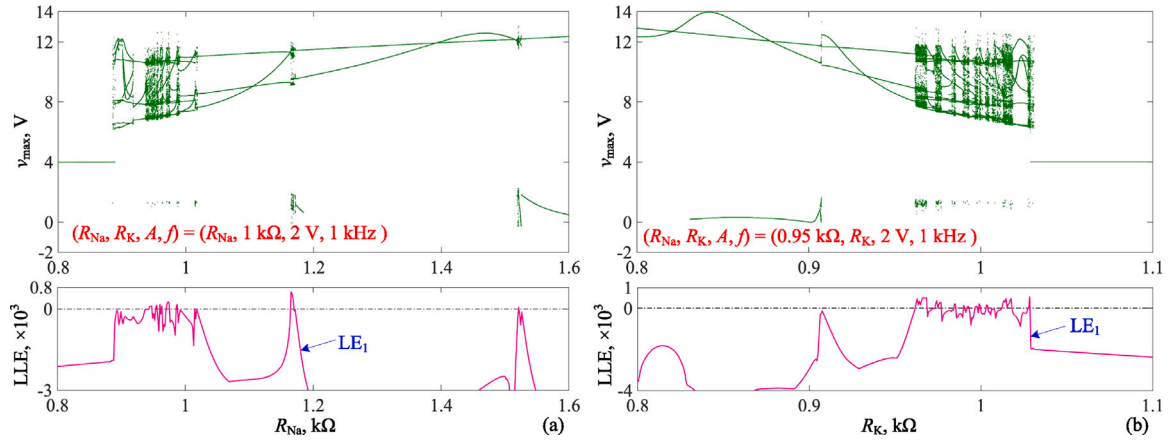


Fig. 5. Bifurcation diagrams and LLE spectra with respect to memristor-related parameters  $R_{Na}$  and  $R_K$ , respectively: (a) for fixed  $R_K = 1$  kΩ,  $R_{Na}$ -related 1D bifurcation diagram (top) and LLE spectrum (bottom); (b) for fixed  $R_{Na} = 0.95$  kΩ,  $R_K$ -related 1D bifurcation diagram (top) and LLE spectrum (bottom).

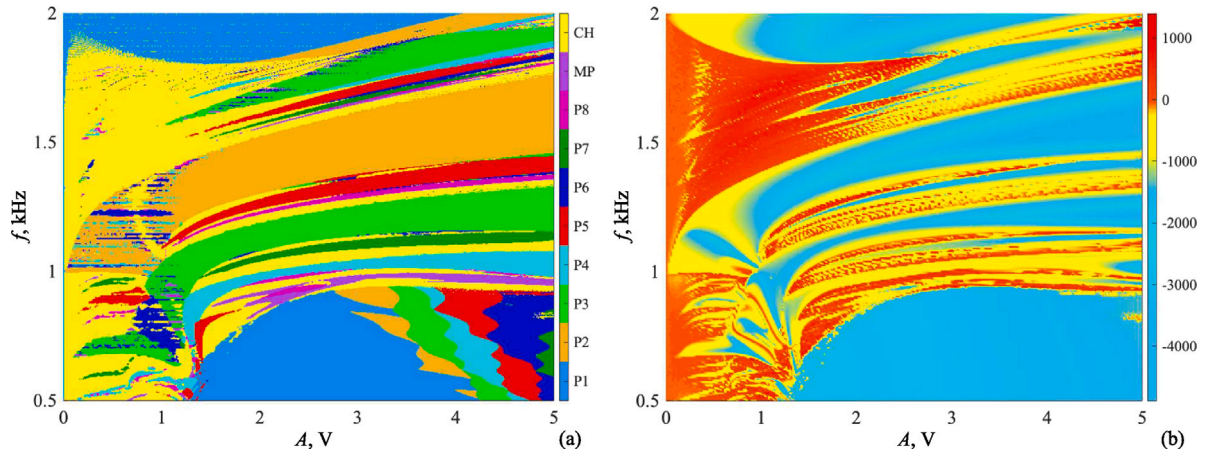


Fig. 6. Stimulus parameter-related dynamical distributions in the  $A$ - $f$  parameter plane: (a) 2D bifurcation diagram depicted by checking the periodicities of membrane potential  $v_i$ ; (b) 2D dynamical map described by LLE. (For interpretation of the references to color in this figure legend, the reader is referred to the web version of this article.)

### 3.3. Parameter-dependent firing patterns

Herein, time-domain waveforms of membrane potential  $v$  and phase portrait in the  $v_{\varphi_3} - v$  phase plane are employed to further demonstrate the parameter-related firing patterns, as shown in Fig. 8. We

only display some firing patterns with respect to different memristor parameters  $R_{Na}$  and amplitude  $A$  as examples.

In Fig. 8(a), time-domain waveforms of the membrane potential  $v$  (left) and phase portraits in the  $v_{\varphi_3} - v$  phase plane (right) are figured out, these are period-8 spiking, period-4 spiking, chaotic spiking, period-3 spiking, and period-2 spiking for  $R_{Na} = 0.9$  kΩ, 0.92 kΩ,

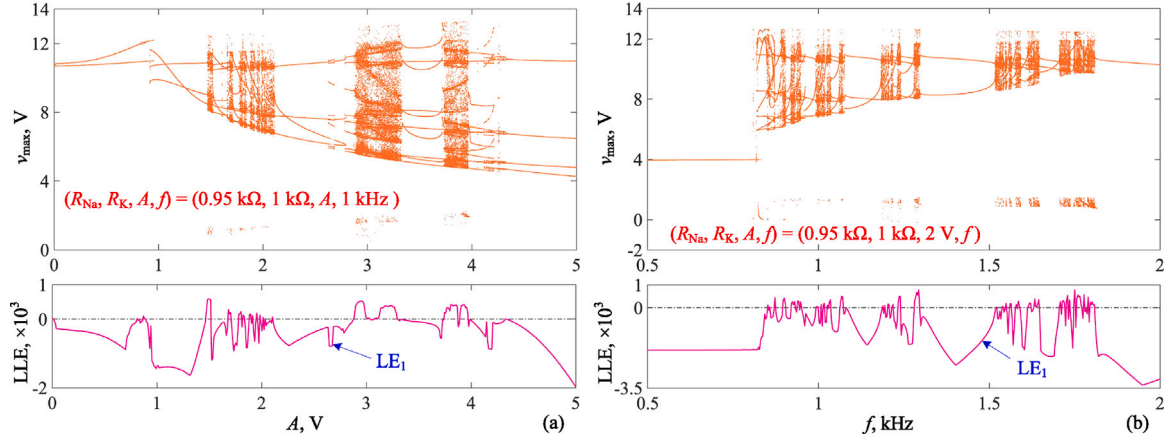


Fig. 7. Stimulus parameter-related bifurcation behaviors with respect to the amplitude and frequency: (a) for fixed  $f = 1$  kHz, the amplitude-related 1D bifurcation diagram (top) and LLE spectrum (bottom); (b) for fixed  $A = 2$  V, the frequency-related 1D bifurcation diagram (top) and LLE spectrum (bottom).

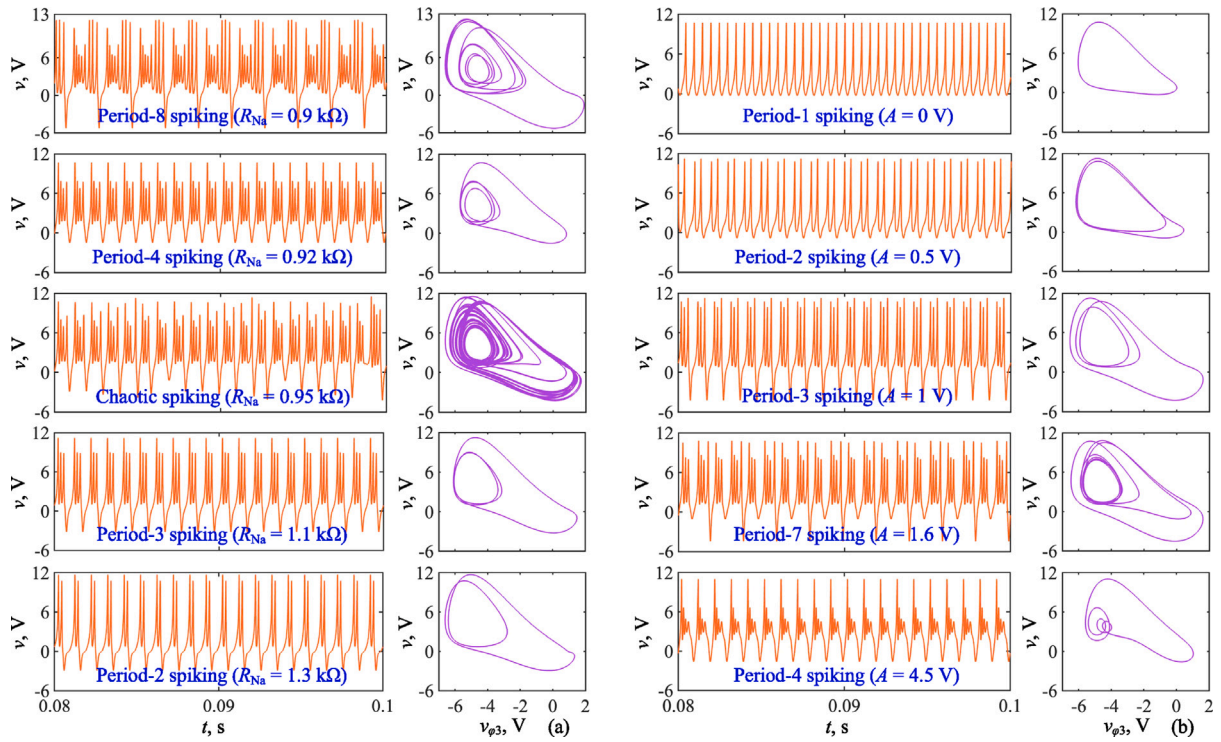


Fig. 8. Time-domain waveforms of the membrane potential  $v$  (left) and phase portraits in the  $v_{p3}$ – $v$  phase plane (right) for  $R_{Na}$ - and amplitude-related firing patterns: (a) period-8 spiking, period-4 spiking, chaotic spiking, period-3 spiking, and period-2 spiking for  $R_{Na} = 0.9$  k $\Omega$ , 0.92 k $\Omega$ , 0.95 k $\Omega$ , 1.1 k $\Omega$ , and 1.3 k $\Omega$ , respectively; (b) period-1 spiking, period-2 spiking, period-3 spiking, period-7 spiking, and period-4 spiking for  $A = 0$  V, 0.5 V, 1 V, 1.6 V, and 4.5 V, respectively.

0.95 k $\Omega$ , 1 k $\Omega$ , 1.3 k $\Omega$ , respectively. For the amplitude-related firing patterns, period-1 spiking, period-2 spiking, period-3 spiking, period-7 spiking, and period-4 spiking for  $A = 0$  V, 0.5 V, 1 V, 1.6 V, and 4.5 V, are respectively depicted in Fig. 8(b). These numerical results demonstrate that the memristive Hodgkin–Huxley circuit can truthfully generate periodic spiking behaviors with different periodicities and chaotic spiking behavior as the original Hodgkin–Huxley circuit do. The spiking firing patterns hold the promise to provide high energy efficient implementations of spike-based neuromorphic hardware for spiking neural networks. Notably, the numerical results further confirm that the electrical characteristics of ion channels and externally applied electrical stimulus can intensively affect the electrophysiological response of biological neurons in human brain.

#### 4. Analog circuit implementation and hardware experiment

The hardware experiments on analog level is a critical way to verify the correctness of numerically simulated firing patterns. Up to date, the Hodgkin–Huxley neurons have been realized by silicon-based very large scale integration (VLSI) circuit [49] and simplified Hodgkin–Huxley neurons have been implemented by memristor devices [26], but memristive Hodgkin–Huxley-like circuit implemented by employing memristor emulator has not been reported. However, the effects of discretization errors should be taken into consideration for digital circuit experiment [69,70]. Besides, inevitable interferences of the parasitic circuit parameters and temperature-drift effects should be considered in analog hardware experiment [21,35,71,72].



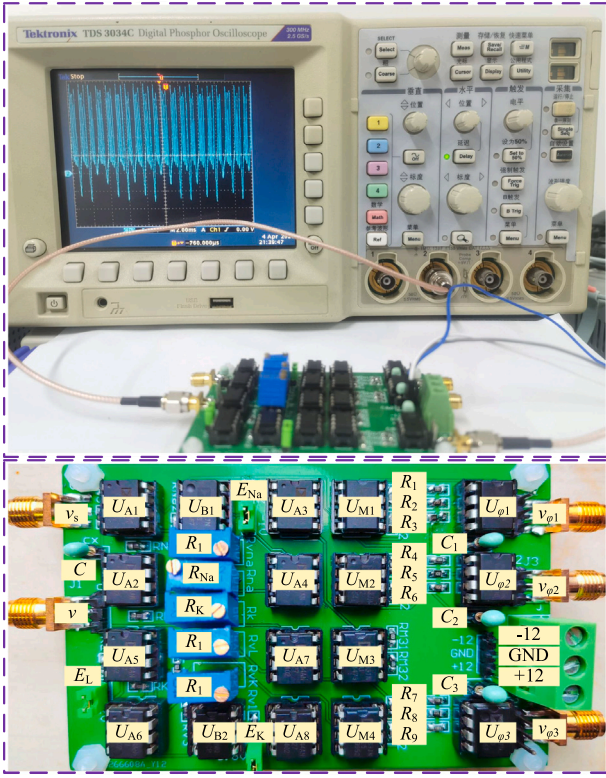


Fig. 9. PCB-based hardware circuit for the memristive Hodgkin-Huxley circuit (bottom) and a snapshot of hardware experimental platform connected with a digital phosphor oscilloscope (up).

#### 4.1. Analog circuit implementation

Thanks to the analog reliability of the two proposed LAMs, the analog circuit implementation for the memristive Hodgkin-Huxley circuit is feasible. This is very critical for the hardware implementation of neuron-based engineering applications. For the analog circuit implementation, active circuit components of operational amplifiers (op-amps) AD711JN/TL082CP, CFOA AD844AN, and analog multiplier AD633JN, as well as passive components of capacitor, potentiometer, and chip resistor are employed. Referring to the circuit schematics in Figs. 1 and 3, a PCB-based hardware circuit of the memristive Hodgkin-Huxley circuit is manually welded, as shown in the bottom of Fig. 9. Note that  $U_{A1}$  to  $U_{A8}$  are CFOA AD844AN,  $U_{\phi1}$  to  $U_{\phi3}$  and  $U_{B1}$  are op-amps AD711JN,  $U_{B2}$  is op-amp TL082CP, and  $U_{M1}$  to  $U_{M4}$  are analog multipliers AD633JN. Besides, the equivalent circuit realizing by integrator [23] can be designed for implementing the dimensionless neuromorphic system deduced from (5). But the hardware circuit realized in this approach is more complicated than the one in Fig. 9.

A hardware experimental platform is set up and a snapshot of the platform is illustrated in the up of Fig. 9. In hardware experiment, an arbitrary function generator is utilized to provide the externally applied stimulus and a 4-channel digital phosphor oscilloscope is employed to display the time-domain waveform of membrane potential, i.e. voltage of capacitor  $C$ . Besides, the hardware circuit is powered by  $\pm 12$  V DC voltage supplies and three voltage converters realized by op-amps  $U_{B1}$  and  $U_{B2}$  are hired to offer the three reversal potentials  $E_{Na}$ ,  $E_K$ , and  $E_L$ , respectively. These reversal potentials are obtained by converting the  $\pm 12$  V DC voltage provided from TPS5420 switching voltage regulator power module and they can be flexible adjusted. This can reduce high frequency burrs of the three reversal potentials and then avoid the burrs of the experimental results.

#### 4.2. Hardware experiment

To verify the time-domain waveforms for the memristor parameter  $R_{Na}$ -related firing patterns in Fig. 8(a) and for the amplitude-related firing patterns in Fig. 8(b), experimental results are captured as shown in Fig. 10 by fine adjusting circuit parameters. Those are, the experimentally captured time-domain waveforms of period-8, period-4, chaotic, period-3, and period-2 spiking firing patterns corresponding to the ones in numerical simulations shown in Fig. 8(a), as well as the experimentally captured time-domain waveforms of period-1, period-2, period-3, period-7, and period-4 spiking firing patterns corresponding to the ones in numerical simulations shown in Fig. 8(b).

The locations of these firing patterns in the captured results are shifted downward by 2 V for good visualization. In hardware experiment, all circuit parameters are set to the ones utilized in the numerical simulations. However, the memristor-related parameters  $R_{Na}$  and  $R_K$ , amplitude of externally applied stimulus  $A$ , and reversal potentials  $E_{Na}$  and  $E_K$  are finely turned during the hardware experiment to counteract the inevitable interferences [22]. These finely turned circuit parameters employed in hardware experiments are listed in Table 1.

It is demonstrated that small deviations are existed between the circuit parameters employed in numerical simulations and the ones utilized in hardware experiments. Pioneer work have proposed that the mean absolute percentage error (MAPE) is an effective method to evaluate the deviations between the parameters utilized in numerical simulations and the ones in experimental measurement [22]. In the pioneer work, MAPE is utilized to evaluate the deviations between the measured and desired resistances. To extend this method, we employ MAPE to evaluate the deviations between all the finely turned parameters in hardware experiments ( $P_{measuredk}$ ) and their desired parameters in numerical simulations ( $P_{desiredk}$ ).

Therefore, the MAPE expression in [21] is rewritten as

$$MAPE = \frac{1}{N} \sum_{k=1}^N \frac{|R_{desiredk} - R_{measuredk}|}{R_{desiredk}} \times 100\%, \quad (6)$$

where  $N$  is the number of finely turned parameters. The measured parameters  $P_{measuredk}$  are listed in Table 1 and the MAPEs are calculated for different cases given with  $N = 4$  for Fig. 10(a) and  $N = 5$  for Fig. 10(b), respectively. The calculated MAPEs are all less than 10%, which is acceptable in the PCB-based hardware experiments. Besides, the experimentally utilized parameter  $R_K$  are slightly smaller than the ones employed in numerical simulation. Whereas that, the experimentally utilized parameter  $R_{Na}$  are slightly bigger than the ones employed in numerical simulation. This can give us the guidance in adjusting the memristive Hodgkin-Huxley circuit to generate expected spiking firing patterns. Ignore these inevitable interferences, the experimentally captured spiking firing patterns can well verify the numerically simulated ones. This illustrates the availability of the proposed memristive Hodgkin-Huxley circuit in generating periodic/chaotic spiking firing patterns.

#### 5. Conclusion

This paper presents a second-order LAM and a first-order LAM to respectively characterize the sodium and potassium ion channels of a neuron. Thereafter, a memristive Hodgkin-Huxley circuit was built and thereby its mathematical model was established. Numerical simulations of the mathematical model and hardware experiments on a PCB-based analog circuit were executed, which demonstrate the generations of abundant firing patterns and coexisting firing patterns in the memristive Hodgkin-Huxley circuit. Consequently, the memristive Hodgkin-Huxley circuit with LAMs described ion channels can effectively reproduce the dynamical behaviors of the firing patterns, i.e. periodic and chaotic firing patterns, in biological neurons. Besides, the memristor emulator-based neuromorphic circuit demonstrates wide parameter range of behaviors. This might overcome the limited cycle

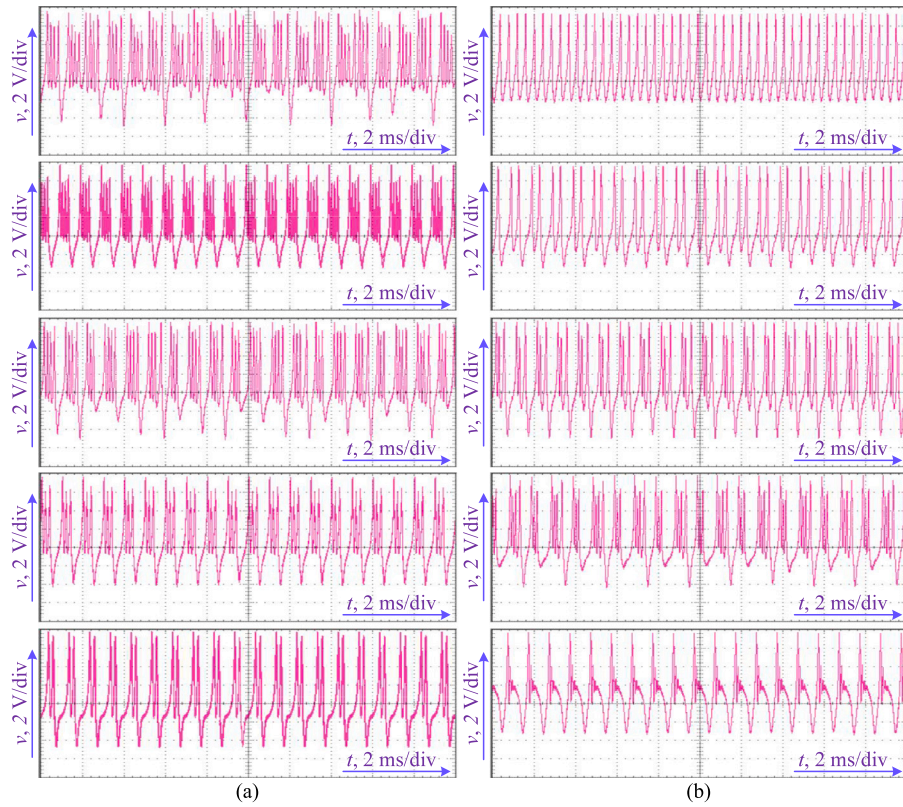


**Fig. 10.** Experimentally measured time-domain waveforms of the membrane potential  $v$  for the memristor parameter  $R_{Na}$ -related firing patterns (left) and amplitude-related firing patterns (right): (a) period-8, period-4, chaotic, period-3, and period-2 spiking firing patterns; (b) period-1, period-2, period-3, period-7, and period-4 spiking firing patterns.

**Table 1**

Coexisting multiple attractors under different initial conditions for different parameters.

Figure	Measured parameters	MAPE
Fig. 10(a) Period-8 spiking	$(R_{Na}, R_K, E_{Na}, E_K) = (0.910 \text{ k}\Omega, 0.789 \text{ k}\Omega, 1.050 \text{ V}, 0.800 \text{ V})$	8.15%
Fig. 10(a) Period-4 spiking	$(R_{Na}, R_K, E_{Na}, E_K) = (0.933 \text{ k}\Omega, 0.786 \text{ k}\Omega, 1.000 \text{ V}, 0.800 \text{ V})$	7.15%
Fig. 10(a) Chaotic spiking	$(R_{Na}, R_K, E_{Na}, E_K) = (1.100 \text{ k}\Omega, 0.800 \text{ k}\Omega, 1.000 \text{ V}, 0.800 \text{ V})$	9.66%
Fig. 10(a) Period-3 spiking	$(R_{Na}, R_K, E_{Na}, E_K) = (1.250 \text{ k}\Omega, 0.830 \text{ k}\Omega, 1.000 \text{ V}, 0.850 \text{ V})$	9.59%
Fig. 10(a) Period-2 spiking	$(R_{Na}, R_K, E_{Na}, E_K) = (1.415 \text{ k}\Omega, 0.778 \text{ k}\Omega, 1.000 \text{ V}, 0.800 \text{ V})$	9.17%
Fig. 10(b) Period-1 spiking	$(A, R_{Na}, R_K, E_{Na}, E_K) = (0.0 \text{ V}, 0.950 \text{ k}\Omega, 0.810 \text{ k}\Omega, 1.160 \text{ V}, 0.800 \text{ V})$	7.45%
Fig. 10(b) Period-2 spiking	$(A, R_{Na}, R_K, E_{Na}, E_K) = (0.5 \text{ V}, 1.070 \text{ k}\Omega, 0.803 \text{ k}\Omega, 1.000 \text{ V}, 0.800 \text{ V})$	7.15%
Fig. 10(b) Period-3 spiking	$(A, R_{Na}, R_K, E_{Na}, E_K) = (1.1 \text{ V}, 1.060 \text{ k}\Omega, 0.884 \text{ k}\Omega, 1.143 \text{ V}, 0.790 \text{ V})$	9.27%
Fig. 10(b) Period-7 spiking	$(A, R_{Na}, R_K, E_{Na}, E_K) = (1.6 \text{ V}, 1.030 \text{ k}\Omega, 0.816 \text{ k}\Omega, 1.000 \text{ V}, 0.840 \text{ V})$	7.02%
Fig. 10(b) Period-4 spiking	$(A, R_{Na}, R_K, E_{Na}, E_K) = (5.4 \text{ V}, 0.950 \text{ k}\Omega, 1.000 \text{ k}\Omega, 1.000 \text{ V}, 0.800 \text{ V})$	3.33%

endurance of neuristor [57]. The memristive neuromorphic circuit employing the proposed first-order LAM and second-order LAM with simple mathematical models was implemented by discrete circuit components, but their implementing circuit are complicated. In future investigation, we will try our best to establish LAMs with simpler mathematical model and analog circuit implementation to characterize the sodium and potassium ion channels. Some future targets will also be focus on employing the physical memristor-based neuromorphic

circuit, as well as developing neuron-based applications and optimizing energy efficiency.

#### CRediT authorship contribution statement

**Quan Xu:** Supervision, Methodology, Writing – original draft. **Yiteng Wang:** Conceptualization, Formal analysis, Experiment. **Bei Chen:** Formal analysis, Writing – review & editing. **Ze Li:** Software. **Ning Wang:** Project administration, Writing – review & editing.



## Declaration of competing interest

The authors declare that they have no known competing financial interests or personal relationships that could have appeared to influence the work reported in this paper.

## Data availability

No data was used for the research described in the article

## Acknowledgments

This work was supported by the grants from the National Natural Science Foundations of China under 12172066 and 61801054, the Natural Science Foundation of Jiangsu Province, China, under BK20160282 and BK20210850, the Project 333 of Jiangsu Province, the Postgraduate Research and Practice Innovation Program of Jiangsu Province, China under Grant No. KYCX23\_3054, and the College Students' Innovation and Entrepreneurship Training Program of Changzhou University.

## References

- [1] Dong Y, Yang S, Liang Y, Wang G. Neuromorphic dynamics near the edge of chaos in memristive neurons. *Chaos Solitons Fractals* 2022;160:112241. <http://dx.doi.org/10.1016/j.chaos.2022.112241>.
- [2] Lu Y, Wang C, Deng Q, Xu C. The dynamics of a memristor-based Rulkov neuron with fractional-order difference. *Chin Phys B* 2022;31:060502. <http://dx.doi.org/10.1088/1674-1056/ac539a>.
- [3] Lin H, Wang C, Yu F, Sun J, Du S, Deng Z, Deng Q. A review of chaotic systems based on memristive Hopfield neural networks. *Mathematics* 2023;11(6):1369. <http://dx.doi.org/10.3390/math11061369>.
- [4] Lin H, Wang C, Cui L, Sun Y, Zhang X, Yao W. Hyperchaotic memristive ring neural network and application in medical image encryption. *Nonlinear Dyn* 2022;110:841–55. <http://dx.doi.org/10.1007/s11071-022-07630-0>.
- [5] Wen Z, Wang C, Deng Q, Lin H. Regulating memristive neuronal dynamical properties via excitatory or inhibitory magnetic field coupling. *Nonlinear Dyn* 2022;110:3823–35. <http://dx.doi.org/10.1007/s11071-022-07813-9>.
- [6] Yu X, Bao H, Chen M, Bao B. Energy balance via memristor synapse in Morris-Lecar two-neuron network with FPGA implementation. *Chaos Solitons Fractals* 2023;171:113442. <http://dx.doi.org/10.1016/j.chaos.2023.113442>.
- [7] Lin H, Wang C, Sun J, Zhang X, Sun Y, H.C. lu H. Memristor-coupled asymmetric neural networks: Bionic modeling, chaotic dynamics analysis and encryption application. *Chaos Solitons Fractals* 2023;166:112905. <http://dx.doi.org/10.1016/j.chaos.2022.112905>.
- [8] Sun G, Yang F, Ren G, Wang C. Energy encoding in a biophysical neuron and adaptive energy balance under field coupling. *Chaos Solitons Fractals* 2023;169:113230. <http://dx.doi.org/10.1016/j.chaos.2023.113230>.
- [9] Kafraj MS, Parastesh F, Jafari S. Firing patterns of an improved Izhikevich neuron model under the effect of electromagnetic induction and noise. *Chaos Solitons Fractals* 2020;137:109782. <http://dx.doi.org/10.1016/j.chaos.2020.109782>.
- [10] Ji X, Hu X, Zhou Y, Dong Z, Duan S. Adaptive sparse coding based on memristive neural network with applications. *Cogn Neurodyn* 2019;13:475–88. <http://dx.doi.org/10.1007/s11571-019-09537-w>.
- [11] Zhu Z, Wang R, Zhu F. The energy coding of a structural neural network based on the Hodgkin–Huxley model. *Front Neurosci* 2018;12:122. <http://dx.doi.org/10.3389/fnins.2018.00122>.
- [12] Ma J, Tang J. A review for dynamics in neuron and neuronal network. *Nonlinear Dyn* 2017;89(3):1569–78. <http://dx.doi.org/10.1007/s11071-017-3565-3>.
- [13] Ma J. Biophysical neurons, energy, and synapse controllability: a review. *J Zhejiang Univ-Sci A* 2023;24(2):109–29. <http://dx.doi.org/10.1631/jzus.A2200469>.
- [14] An X, Qiao S. The hidden, period-adding, mixed-mode oscillations and control in a HR neuron under electromagnetic induction. *Chaos Solitons Fractals* 2021;143:110587. <http://dx.doi.org/10.1016/j.chaos.2020.110587>.
- [15] Xu Q, Tan X, Zhu D, Bao H, Hu Y, Bao B. Bifurcations to bursting and spiking in the Chay neuron and their validation in a digital circuit. *Chaos Solitons Fractals* 2020;141:110353. <http://dx.doi.org/10.1016/j.chaos.2020.110353>.
- [16] Panahi S, Jafari S, Khalaf AJM, Rajagopal K, Pham VT, Alsaadi FE. Complete dynamical analysis of a neuron under magnetic flow effect. *Chin J Phys* 2018;56(5):2254–64. <http://dx.doi.org/10.1016/j.cjph.2018.08.008>.
- [17] Gu H, Pan B, Chen G, Duan L. Biological experimental demonstration of bifurcations from bursting to spiking predicted by theoretical models. *Nonlinear Dyn* 2014;78(1):391–407. <http://dx.doi.org/10.1007/s11071-014-1447-5>.
- [18] Lin H, Wang C, Deng Q, Xu C, Deng Z, Zhou C. Review on chaotic dynamics of memristive neuron and neural network. *Nonlinear Dyn* 2021;110(4):3807–22. <http://dx.doi.org/10.1007/s11071-021-06853-x>.
- [19] Nguetcho AST, Binczak S, Kazantsev VB, Jacquir S, Bilbault J-M. Experimental active spike response of analog electrical neuron: beyond “integrate-and-fire” transmission. *Nonlinear Dyn* 2015;82(3):1595–604. <http://dx.doi.org/10.1007/s11071-015-2263-2>.
- [20] Xu Q, Zhu D. FPGA-based experimental validations of electrical activities in two adjacent FitzHugh-Nagumo neurons coupled by memristive electromagnetic induction. *IETE Tech Rev* 2020;38(6):563–77. <http://dx.doi.org/10.1080/02564602.2020.1800526>.
- [21] Cai J, Bao H, Xu Q, Hua Z, Bao B. Smooth nonlinear fitting scheme for analog multiplierless implementation of Hindmarsh-Rose neuron model. *Nonlinear Dyn* 2021;104(4):4379–89. <http://dx.doi.org/10.1007/s11071-021-06453-9>.
- [22] Xu Q, Chen X, Chen B, Wu H, Li Z, Bao H. Dynamical analysis of an improved FitzHugh-Nagumo neuron model with multiplier-free implementation. *Nonlinear Dyn* 2023;111(9):8737–49. <http://dx.doi.org/10.1007/s11071-023-08274-4>.
- [23] Ding S, Wang N, Bao H, Chen B, Wu H, Xu Q. Memristor synapse-coupled piecewise-linear simplified Hopfield neural network: Dynamics analysis and circuit implementation. *Chaos Solitons Fractals* 2023;166:112899. <http://dx.doi.org/10.1016/j.chaos.2022.112899>.
- [24] Basu A, Ramakrishnan S, Petre C, Kozioł S, Brink S, Hasler PE. Neural dynamics in reconfigurable silicon. *IEEE Trans Biomed Circuits Syst* 2010;4(5):311–9. <http://dx.doi.org/10.1109/TBCAS.2010.2055157>.
- [25] Basu A, Hasler PE. Nullcline-based design of a silicon neuron. *IEEE Trans Circuits Syst I* 2010;57(11):2938–47. <http://dx.doi.org/10.1109/TCSI.2010.2048772>.
- [26] Pickett MD, Medeiros-Ribeiro G, Williams RS. A scalable neuristor built with Mott memristors. *Nature Mater* 2013;12(2):114–7. <http://dx.doi.org/10.1038/nmat3510>.
- [27] Kang SM, Choi D, Eshraghian JK, Zhou P, Kim J, Kong BS, Zhu X, Demirkol AS, Ascoli A, Tetzlaff R, Lu W, Chua LO. How to build a memristive integrate-and-fire model for spiking neuronal signal generation. *IEEE Trans Circuits Syst I* 2021;68(12):4837–50. <http://dx.doi.org/10.1109/TCSI.2021.3126555>.
- [28] Rao A, Plank P, Wild A, Maass W. A long short-term memory for AI applications in spike-based neuromorphic hardware. *Nat Mach Intell* 2022;4:467–79. <http://dx.doi.org/10.1038/s42256-022-00480-w>.
- [29] Xu Q, Ding S, Bao H, Chen M, Bao B. Piecewise-linear simplification for adaptive synaptic neuron model. *IEEE Trans Circuits and Syst II* 2022;69(3):1832–6. <http://dx.doi.org/10.1109/TCSII.2021.3124666>.
- [30] Shen H, Yu F, Wang C, Sun J, Cai S. Firing mechanism based on single memristive neuron and double memristive coupled neurons. *Nonlinear Dyn* 2022;106(1):959–73. <http://dx.doi.org/10.1007/s11071-022-07812-w>.
- [31] Njitacke ZT, Takembo CN, Awrejcewicz J, Fouda HPE, Kengne J. Hamilton energy, complex dynamical analysis and information patterns of a new memristive FitzHugh-Nagumo neural network. *Chaos Solitons Fractals* 2022;160:112211. <http://dx.doi.org/10.1016/j.chaos.2022.112211>.
- [32] Xu Q, Liu T, Ding S, Bao H, Li Z, Chen B. Extreme multistability and phase synchronization in a heterogeneous bi-neuron Rulkov network with memristive electromagnetic induction. *Cogn Neurodyn* 2022. <http://dx.doi.org/10.1007/s11571-022-09866-3>.
- [33] Li Z, Guo Z, Wang M, Ma M. Firing activities induced by memristive autapse in Fitzhugh-Nagumo neuron with time delay. *AEÜ-Int J Electron Commun* 2021;142:153995. <http://dx.doi.org/10.1016/j.aeue.2021.153995>.
- [34] Xu Q, Ju Z, Ding S, Feng C, Chen M, Bao B. Electromagnetic induction effects on electrical activity within a memristive Wilson neuron model. *Cogn Neurodyn* 2022;16:1221–31. <http://dx.doi.org/10.1007/s11571-021-09764-0>.
- [35] Xu Q, Liu T, Feng C, Bao H, Wu H, Bao B. Continuous non-autonomous memristive Rulkov model with extreme multistability. *Chin Phys B* 2021;30(12):128702. <http://dx.doi.org/10.1088/1674-1056/ac2f30>.
- [36] Sah PM, Kim H, Chua LO. Brains are made of memristor. *IEEE Trans Circ Syst Mag* 2014;14(1):12–36. <http://dx.doi.org/10.1109/MCAS.2013.2296414>.
- [37] Sung SH, Kim TJ, Shin H, Im TH, Lee KJ. Simultaneous emulation of synaptic and intrinsic plasticity using a memristive synapse. *Nature Commun* 2022;13:2811. <http://dx.doi.org/10.1038/s41467-022-30432-2>.
- [38] Sun J, Wang Y, Liu P, Wen S, Wang Y. Memristor-based neural network circuit with multimode generalization and differentiation on pavlov associative memory. *IEEE Trans Cybern* 2023;53(5):3351–62. <http://dx.doi.org/10.1109/TCYB.2022.3200751>.
- [39] Chua LO. Hodgkin–Huxley equations implies edge of chaos kernel. *Jpn J Appl Phys* 2022;61:SM0805. <http://dx.doi.org/10.35848/1347-4065/ac64e1>.
- [40] Chua LO, Sbitnev V, Kim H. Neurons are poised near the edge of chaos. *Int J Bifurcation Chaos* 2012;22(4):1250098. <http://dx.doi.org/10.1142/S0218127412500988>.
- [41] Lu Z, Liang Y, Dong Y, Wang S. Spiking and chaotic behaviors of locally active memristor-based neuron circuit. *Electron Lett* 2022;58(18):681–3. <http://dx.doi.org/10.1049/ell2.12567>.
- [42] Weiher M, Herzog M, Tetzlaff R, Ascoli A, Mikolajick T, Slesazek S. Pattern formation with locally active S-type NbOx memristors. *IEEE Trans Circuits Syst I* 2019;66(7):2627–38. <http://dx.doi.org/10.1109/TCSI.2019.2894218>.

- [43] Mannan ZI, Yang C, Kim H. Oscillation with 4-lobe Chua corsage memristor. *IEEE Trans Circ Syst Mag* 2018;18(2):14–27. <http://dx.doi.org/10.1109/MCAS.2018.2821724>.
- [44] Jin P, Wang G, Liang Y, Iu HH-C, Chua LO. Neuromorphic dynamics of Chua corsage memristor. *IEEE Trans Circ Syst I* 2021;68(11):4419–32. <http://dx.doi.org/10.1109/TCSI.2021.3121676>.
- [45] Dong Y, Yang S, Liang Y, Wang G. Neuromorphic dynamics near the edge of chaos in memristive neurons. *Chaos Solitons Fractals* 2022;160:112241. <http://dx.doi.org/10.1016/j.chaos.2022.112241>.
- [46] Tan Y, Wang C. A simple locally active memristor and its application in HR neurons. *Chaos* 2020;30:053118. <http://dx.doi.org/10.1063/1.5143071>.
- [47] Hodgkin AL, Huxley AF. A quantitative description of membrane current and its application to conduction and excitation in nerve. *J Physiol* 1952;117(4):500–44. <http://dx.doi.org/10.1113/jphysiol.1952.sp004764>.
- [48] Hodgkin AL. The ionic basis of electrical activity in nerve and muscle. *Biol Rev* 1951;26(4):339–409. <http://dx.doi.org/10.1111/j.1469-185X.1951.tb01204.x>.
- [49] Saighi S, Bornat Y, Tomas J, Masson GL, Renaud S. A library of analog operators based on the Hodgkin–Huxley formalism for the design of tunable, real-time, silicon neurons. *IEEE Trans Biomed Circuits Syst* 2011;5(1):3–19. <http://dx.doi.org/10.1109/TBCAS.2010.2078816>.
- [50] Yu T, Cauwenberghs G. Analog VLSI biophysical neurons and synapses with programmable membrane channel kinetics. *IEEE Trans Biomed Circuits Syst* 2010;4(3):139–48. <http://dx.doi.org/10.1109/TBCAS.2010.2048566>.
- [51] Huang H, Yang R, Tan Z, He H, Zhou W, Xiong J, Guo X. Quasi-Hodgkin-Huxley neurons with leaky integrate-and-fire functions physically realized with memristive devices. *Adv Mater* 2019;31(3):1803849. <http://dx.doi.org/10.1002/adma.201803849>.
- [52] Haghir S, Naderi A, Ghanbari B, Ahmadi A. High speed and low digital resources implementation of Hodgkin-Huxley neuronal model using base-2 functions. *IEEE Trans Circuits Syst I* 2021;68(1):275–87. <http://dx.doi.org/10.1109/TCSI.2020.3026076>.
- [53] Minati L. Simulation versus experiment in non-linear dynamical systems. *Chaos Solitons Fractals* 2021;144:110656. <http://dx.doi.org/10.1016/j.chaos.2021.110656>.
- [54] Minati L, Mancinelli M, Frasca M, Bettotti P, Pavesi L. An analog electronic emulator of non-linear dynamics in optical microring resonators. *Chaos Solitons Fractals* 2021;153:111410. <http://dx.doi.org/10.1016/j.chaos.2021.111410>.
- [55] Chua LO. Memristor, Hodgkin-Huxley, and edge of chaos. *Nanotechnology* 2013;24:383001. <http://dx.doi.org/10.1088/0957-4484/24/38/383001>.
- [56] Chua LO. Local activity is the origin of complexity. *Int J Bifurcation Chaos* 2005;15(11):3435–56. <http://dx.doi.org/10.1142/s0218127405014337>.
- [57] Zhou P, Eshraghian JK, Choi DU, Lu WD, Kang SM. Gradient-based neuromorphic learning on dynamical RRAM arrays. *IEEE J Emerg Sel Top Circuits Syst* 2022;12(4):888–97. <http://dx.doi.org/10.1109/JETCAS.2022.3224071>.
- [58] Yu D, Iu HH-C, Fitch AL, Liang Y. A floating memristor emulator based relaxation oscillator. *IEEE Trans Circuits Syst I* 2014;61(10):2888–96. <http://dx.doi.org/10.1109/TCSI.2014.2333687>.
- [59] Tagne kouna IB, Moukam kakmeni FM, Yamapi R. Birhythmic oscillations and global stability analysis of a conductance-based neuronal model under ion channel fluctuations. *Chaos Solitons Fractals* 2022;159:112126. <http://dx.doi.org/10.1016/j.chaos.2022.112126>.
- [60] Kim JH, Lee J-K, Kim H-G, Kim K-B, Kim1 HR. Possible effects of radio frequency electromagnetic field exposure on central nerve system. *Biomol Ther* 2019;27(3):265–75. <http://dx.doi.org/10.4062/biomolther.2018.152>.
- [61] Yu F, Shen H, Yu Q, Kong X, Sharma PK, Cai S. Privacy protection of medical data based on multi-scroll memristive hopfield neural network. *IEEE Trans Netw Sci Eng* 2023;10:845–58. <http://dx.doi.org/10.1109/TNSE.2022.3223930>.
- [62] Yao Y, Ma J. Weak periodic signal detection by sine-Wiener-noise-induced resonance in the FitzHugh-Nagumo neuron. *Cogn Neurodyn* 2018;12:343–9. <http://dx.doi.org/10.1007/s11571-018-9475-3>.
- [63] Sachdeva PS, Livezey JA, DeWeese MR. Heterogeneous synaptic weighting improves neural coding in the presence of common noise. *Neural Comput* 2020;32:1239–76. [http://dx.doi.org/10.1162/neco\\_a\\_01287](http://dx.doi.org/10.1162/neco_a_01287).
- [64] Lu L, Jia Y, Xu Y, Ge M, Yang L, Zhan X. Energy dependence on modes of electric activities of neuron driven by different external mixed signals under electromagnetic induction. *Sci China Technol Sci* 2019;62:427–40. <http://dx.doi.org/10.1007/s11431-017-9217-x>.
- [65] Rajagopal K, Jafari S, Karthikeyan A, Srinivasan A. Effect of magnetic induction on the synchronizability of coupled neuron network. *Chaos* 2021;31(8):083115. <http://dx.doi.org/10.1063/5.0061406>.
- [66] Steyn-Ross DA, Steyn-Ross ML, Wilson MT, Sleight JW. White-noise susceptibility and critical slowing in neurons near spiking threshold. *Phys Rev E* 2006;74:051920. <http://dx.doi.org/10.1103/PhysRevE.74.051920>.
- [67] Jin W, Wang A, Ma J, Lin Q. Effects of electromagnetic induction and noise on the regulation of sleep wake cycle. *Sci China Technol Sci* 2019;62:2113–9. <http://dx.doi.org/10.1007/s11431-018-9423-x>.
- [68] Parastesh F, Rajagopal K, Karthikeyan A, Alsaedi A, Hayat T, Pham V-T. Complex dynamics of a neuron model with discontinuous magnetic induction and exposed to external radiation. *Cogn Neurodyn* 2018;12:607–14. <http://dx.doi.org/10.1007/s11571-018-9497-x>.
- [69] Wang N, Zhang G, Kuznetsov N, Li H. Generating grid chaotic sea from system without equilibrium point. *Commun Nonlinear Sci Numer Simul* 2022;107:106194. <http://dx.doi.org/10.1016/j.cnsns.2021.106194>.
- [70] Yang Y, Huang L, Kuznetsov N, Chai B, Guo Q. Generating multiwing hidden chaotic attractors with only stable node-foci: Analysis, implementation, and application. *IEEE Trans Ind Electron* 2023. <http://dx.doi.org/10.1109/TIE.2023.3273242>.
- [71] Wang N, Li C, Bao H, Chen M, Bao B. Generating multi-scroll Chua's attractors via simplified piecewise-linear Chua's diode. *IEEE Trans Circuits Syst I* 2019;66:4767–79. <http://dx.doi.org/10.1109/TCSI.2019.2933365>.
- [72] Wang N, Xu D, Kuznetsov NV, Bao H, Chen M, Xu Q. Experimental observation of hidden Chua's attractor. *Chaos Solitons Fractals* 2023;170:113427. <http://dx.doi.org/10.1016/j.chaos.2023.113427>.